Supporting Information

From Well-Entangled to Partially-Entangled Wormlike Micelles

Weizhong Zou[#], Grace Tan[#], Hanqiu Jiang[‡], Karsen Vogtt[‡], Michael Weaver[+], Peter Koenig[+], Gregory Beaucage[‡], and Ronald G. Larson[#*]

 # Chemical Engineering, University of Michigan, Ann Arbor, MI 48109

‡ Biomedical, Chemical, and Environmental Engineering, University of Cincinnati, Cincinnati, OH 45221

+ The Procter & Gamble Company, Mason, OH 45040

**Correspondence: email: rlarson@umich.edu, phone: (734) 936-0772, FAX: (734) 763-0459*

In this material, some experimental and simulation details are laid out. For simulations, a flow chart laying out the steps to predict the linear rheological G' and G" curves is presented followed by a complete description of the optimization procedure and sensitivity studies for parameter estimation. For the experiments, the method of combining the macro- and micro- rheological data is elaborated. Finally, the self-recombination associated expressions for the ratio ς_{DC} of micelle diffusion time to recombination time for both entangled and unentangled regimes are also derived in detail.

Simulation procedure. As we discussed briefly in the main text, the specific types of relaxation dynamics a micelle undergoes are strongly affected by its length. According to Table 1, due to the exponential length distribution, micelles in a sufficiently large ensemble can be classified into

three subpopulations, namely, very short unentangled micelle rods ($L_i \leq l_p$), unentangled short, but flexible WLMs ($l_p < L_i < l_e$), and entangled long WLMs ($L_i \geq l_e$). The micelles in the former two groups relax quickly through rotary, Rouse, and bending motions, whose contributions are only significant at high frequencies. To simulate these dynamics explicitly would require lengthy and costly computations, and would require time steps too short to allow runs long enough to account for the much slower reptation of those long entangled WLMs. Therefore, the dynamics of these relatively short micelles are treated analytically (See Eq. 1, and 2) and the results are added directly to the predicted G' and G" curves at the end of each simulation.

For partially entangled WLMs, the ensemble is thus divided into entangled and unentangled micelles. For the entangled micelles, pointers are assigned to track the loss of tube segments in the same way as for the well-entangled system.[32,33] For the unentangled short micelles, however, no pointers are needed, and the micelles are treated as relaxed during the entire simulation (although the contributions from high-frequency Rouse and bending modes from these micelles are included after the simulation finishes, just as is done for entangled micelles). The unentangled micelles do participate in micelle breakage and re-formation, adding their relaxed lengths to each other and to entangled micelles by fusion. Finally, the unrelaxed tube fraction $\mu(t)$ is calculated through summing unrelaxed tube segments between neighboring pointers, and converted into the stress relaxation function $\mu^2(t)$, where the square takes into account for the effect of tube rearrangement. This is then transformed into G' and G" curves accounting for the low and moderate frequency behavior contributed by the entangled WLM subpopulations.[32,33] The high frequency rotary and bending mode contributions are then added for the unentangled micelles shorter than one

persistence length, and these modes plus Rouse modes are added for untangled micelles longer than a persistence length. The local Rouse and bending modes are also added for the entangled micelles. The above simulation scheme is illustrated in the following flow chart:

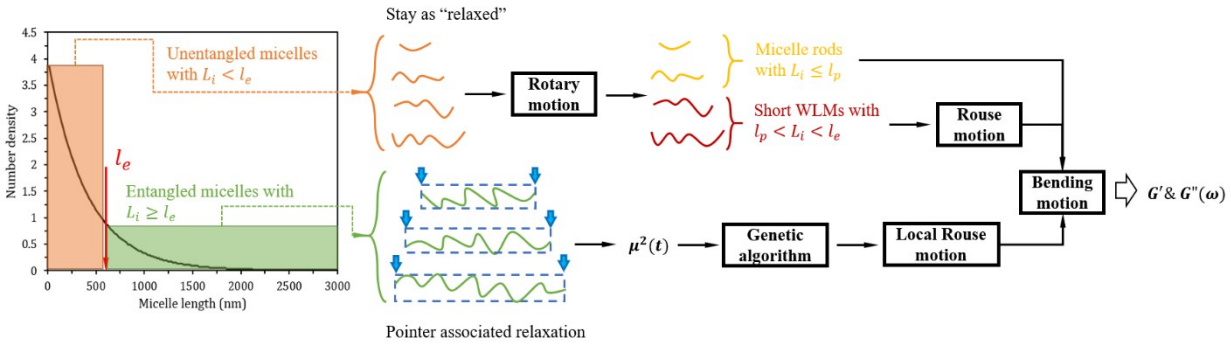

Figure S1. Simulation flow chart for predicting linear rheological behavior of a solution containing both entangled and unentangled micelles.

Merging data from mechanical rheology and DWS. When combining the high-frequency rheological data from DWS with the lower-frequency data from mechanical rheometry, ideally, the two sets of data should overlap at intermediate frequencies (10~100 rad/s). However, pronounced discrepancies are almost always found for WLM solutions at high surfactant or salt concentrations.[33] It is now well accepted that the micro-rheology over- or underestimates the elastic modulus due to slip and the compression of fluid at the interface between particle probe and viscoelastic medium as well as the formation of particle-micelle aggregates.[27,48] As a consequence, to merge DWS data with the mechanical data requires that the magnitudes of G' and G" from DWS be shifted by a factor that depends on the specific frequency range over which the

two data sets overlap. The following procedure is therefore used to obtain the combined G' and G" curves: As shown in Fig. S2, we first remove mechanical rheometric data outside of a frequency window of 0.5-100 rad/s since outside of this range the data are subject either to the effect of inertia (at high frequency) or to low signal-to-noise ratio (at low frequency, where G'<< G"). Analogously, truncation of DWS data is carried out at low (<10 rad/s) and high frequency (>20000 rad/s) due to the poorly resolved terminal behavior of DWS data at low frequencies and the limitation of Brownian motions of probe particles at high frequencies, respectively. The remaining DWS data is then shifted vertically to allow for the best overlap with those from mechanical rheometry at frequencies between 50 to 150 rad/s.

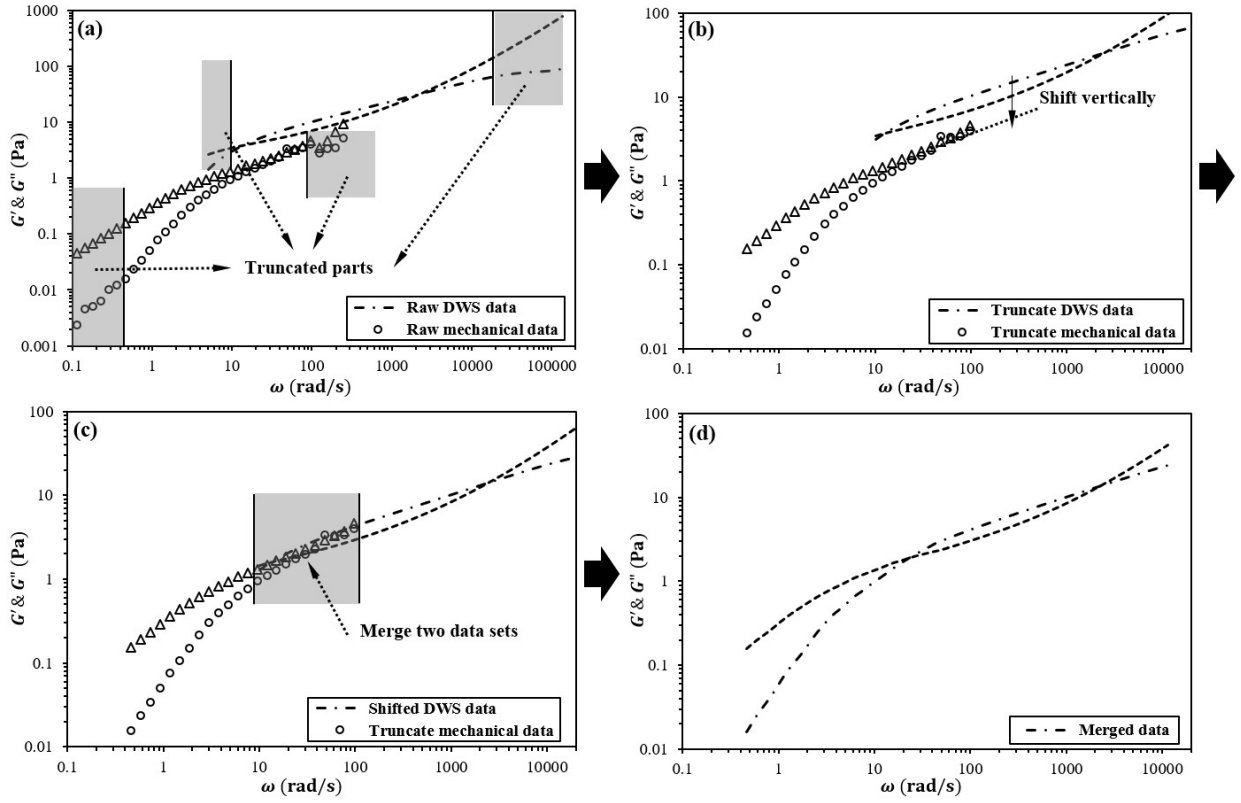

Figure S2. Illustration of the data merging process to combine mechanical rheometric and DWS data.

Parameter optimization. As illustrated by Fig. 2 in the main text, only weak elasticity with negligible effect of breakage and re-formation are exhibited for partially entangled WLM solutions. This leads to low-frequency relaxation behavior that deviates from a single Maxwell model as well as an ill-defined plateau regime at intermediate frequencies, resulting in the disappearance of the local maximum and minimum in G" or, equivalently, of the "dip" in the Cole-Cole plot (i.e., a plot of G" vs G'). Thus, instead of using those local rheological features to fit parameters as we have done for well entangled micelles, we now divide the overall frequency range in a more general way as shown by Fig. S3.

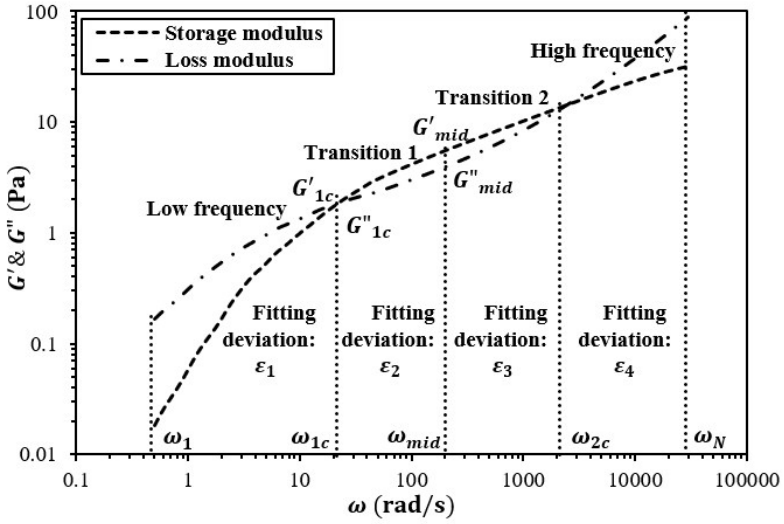

Figure S3. The division of linear rheological G' and G" data into multiple frequency regions for partially entangled WLM solutions. Here $\omega_{mid} = \sqrt{\omega_{1c}\omega_{2c}}$ is the geometric mean of the two crossovers frequencies with G'_{mid},G''_{mid} being the corresponding magnitudes of G' and G" at this

mean frequency, while ω_1 and ω_N are the frequencies corresponding to the first and last data point in the data set, respectively.

In the above figure, the fitting deviations are defined as

$$\varepsilon_j = \frac{1}{N_j}\sum\left\{w_1 log\left[\frac{G'_{fit}(\omega_i)}{G'_{exp}(\omega_i)}\right] + w_2 log\left[\frac{G''_{fit}(\omega_i)}{G''_{exp}(\omega_i)}\right]\right\} \qquad (S1)$$

where N_j is the number of data points in region j, and the subscripts "fit" and "exp" represent the simulated and the experimentally measured data, respectively. The $w_{1,2}$ are weight factors, which we set to $w_1 = w_2 = 1$, except for partially unentangled solutions at frequencies below the low-frequency crossover of G' and G" curves where we set $w_2 = 1.5$, $w_1 = 0.5$ due to the weak signal of G' at low frequencies. The "log" is a base-10 logarithm. The summation in Eq. S1 is over all data points in region j. Note that the sign of ε_j is retained to allow for micellar parameters to be adjusted either upward or downward. After determining ε_j at the end of each iteration, the micellar parameters for generating G' and G" curves during the next iteration are updated with the following empirical correlations:

$$\begin{cases} well\ entangled: \bar{Z}^{k+1} = \bar{Z}^k\left(\dfrac{G'^{exp}_{mid}\, G''^{\,k}_{mid}}{G''^{exp}_{mid}\, G'^{\,k}_{mid}}\right) \\ partially\ entangled: \bar{Z}^{k+1} = \left(\bar{Z}^k - \bar{Z}_c\right)\left(\dfrac{\omega^{exp}_{mid}\omega^{k,fit}_{1c}}{\omega^{exp}_{1c}\omega^{k,fit}_{mid}}\right)^{0.4} + \bar{Z}_c \end{cases} \qquad (S2a)$$

$$G^{k+1}_N = G^k_N\left(\frac{G''^{exp}_{1c}}{G''^{k,fit}_{1c}}\right) \qquad (S2b)$$

$$l^{k+1}_p = l^k_p \sqrt[3]{\omega^{k,fit}_{mid}/\omega^{exp}_{mid}} \qquad (S2c)$$

$$\varsigma^{k+1} = \varsigma^{k}\left[\frac{\omega_{1c}^{k,fit}}{\omega_{1c}^{exp}}\left(\frac{l_p^k \quad \bar{Z}^k}{l_p^{k+1}\bar{Z}^{k+1}}\right)^3\right]^{1.5} \qquad (S2d)$$

Note that the definitions of ω_{1c}, G'_{1c},G''_{1c},ω_{mid},G'_{mid},G''_{mid} can be found in Fig. S3. This scheme for updating parameters is adapted from our previous work, where it was found to lead to rapid convergence, which is needed since each iteration of the fitting procedure requires a simulation using the Pointer Algorithm.

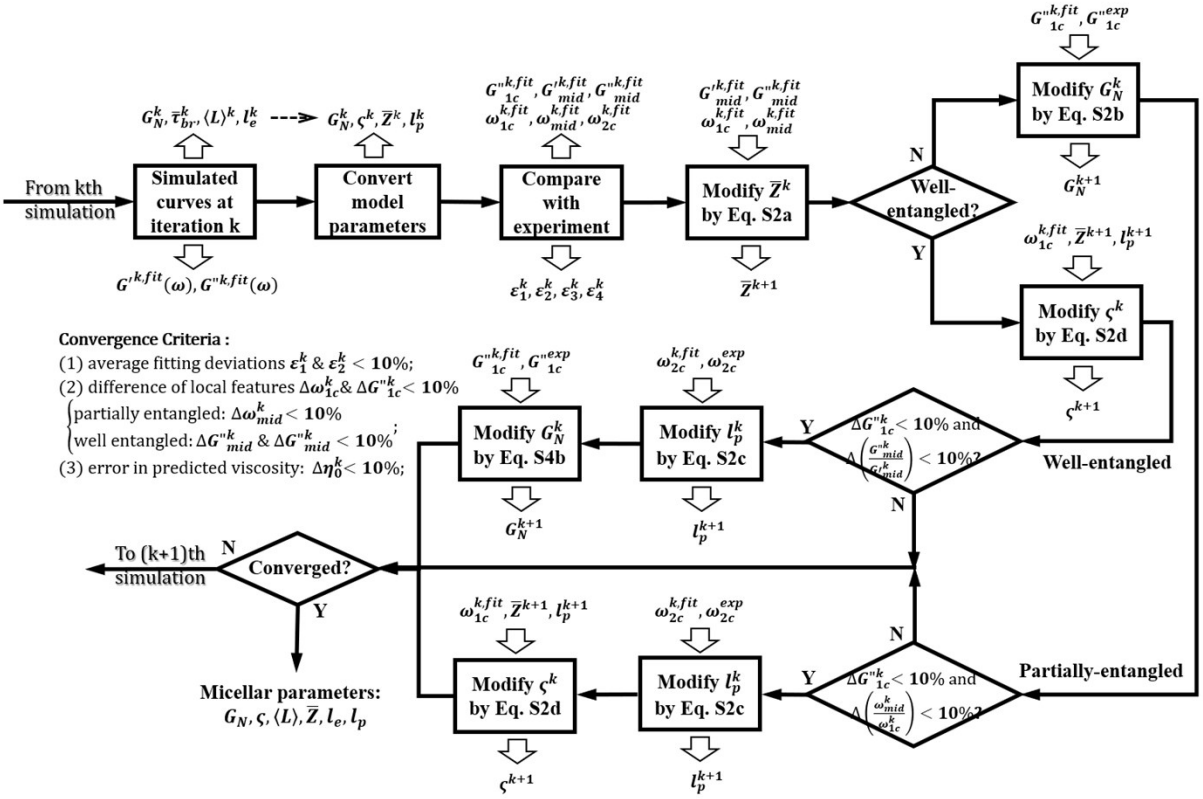

Figure S4. Flow chart of the parameter optimization procedure.

Here, k is iteration number. Details regarding these empirical formulas can be found in the main text and references.[32,33] The optimization process is summarized in Fig. S4. After each simulation,

the fitting deviations ε_j as well as local rheological features are obtained with model parameters updated according to Eq. S2. Different optimization paths are chosen on the basis of whether the solution is partially or well entangled. The iteration eventually stops once a best-fit to experimental data is achieved. Since an appropriate correction of a particular micelle parameter depends on both the sensitivity and the correlation to the other parameters, some parameters will not be optimized as many times as the others over the entire iterations: for example, l_p will be modified only if specific criteria are fulfilled signaling the necessity of changing this parameter for a better fit to experimental data. Thus, with the above procedure, the following best-fits to rheometric data of WLM solutions with [Na+]= 0.651 M, 0.701 M, 0.751 M, and 0.800 M total cation concentration are obtained as shown in Fig. S5. Note in the flow chart that only the errors in regions 1 and 2 are used to assess final convergence, while local features of the G' and G'' curves, i.e., ω_{mid},G'_{mid},G''_{mid} (See Fig. S3), are used to assess convergence in regions 3 and 4.

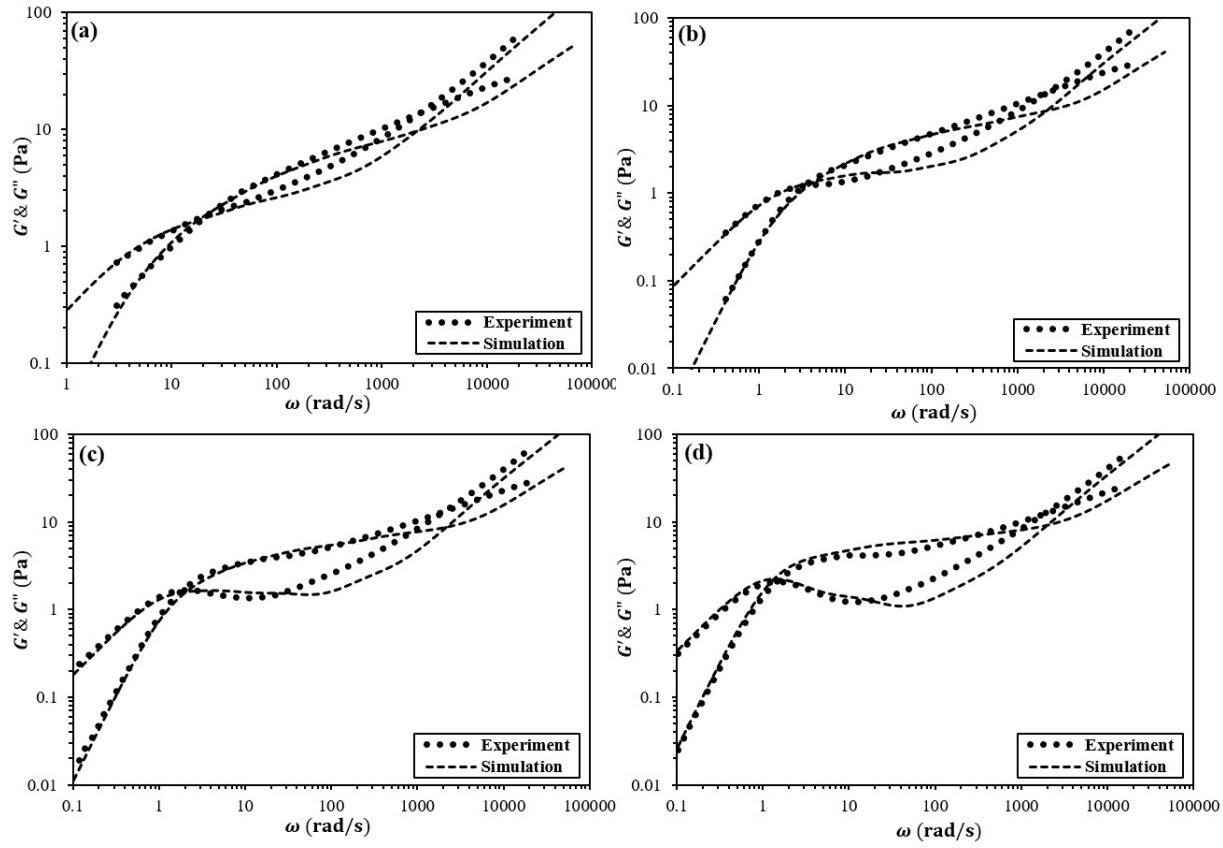

Figure S5. Linear rheological measurements with the corresponding best-fits from simulations for (1.5 wt. % SLE1S+CAPB) micelle solutions at 25 C with different [Na+] which includes contributions from both the counterion for the surfactant and from the added salt: (a) [Na+]=0.651 M; (b) [Na+]=0.701 M; (c) [Na+]=0.751 M; (d) [Na+]=0.800 M. Note that the poor fits at high frequencies do not affect the determination of micelle parameters as long as the high-frequency crossover frequencies are well-matched between the experiment and the simulations, as explained in the discussion of Fig. 5b in the main text.

Sensitivity studies. Although our parameter optimization procedure shows good accuracy and robustness in estimating micellar properties with less than 10% average fitting errors for the local

rheological features (i.e., cross-over frequencies with their associated modulus, ω_{1c}, G''_{1c},ω_{2c} and the corresponding midpoints between them ω_{mid}, G'_{mid},G''_{mid}), as well for the G' and G" curves themselves at low and intermediate frequencies, and for the predicated vs. experimental viscosities (see Fig. S5 for the detailed convergence criteria), some uncertainties in the obtained values of parameters occur as shown by the insensitivity percentage in the main text (See Table 3). Below, the results of sensitivity studies for parameters G_N, ς, $\bar{Z}$, $\langle L \rangle$, l_e, including estimates of parameters and their corresponding fits with/without fixed l_p, are tabulated.

Table S1. Sensitivity study of $\bar{Z}$. Parameter values obtained by best fitting rheological data with unconstrained l_p, with $\bar{Z}$ held at the imposed values of $\bar{Z}$ that vary according to the given percentages from the unconstrained best-fit value, with the corresponding fits of rheological data shown in Fig. S6a.

Parameters	95% $\bar{Z}$	97% $\bar{Z}$	99% $\bar{Z}$	Best-fit	103% $\bar{Z}$	107% $\bar{Z}$	113% $\bar{Z}$
$\bar{Z}$	2.66	2.72	2.79	2.83	2.91	3.00	3.16
$l_e\,(nm)$	406	482	420	403	395	363	376
$l_p\,(nm)$	30.1	24	28.6	30.1	30.1	35.7	36.8
ς	170	193	161	178	119	22	6
$G_N\,(Pa\cdot s)$	13.6	13.07	13.6	13.77	14.30	13.61	12.32
$\langle L\rangle\,(\mu m)$	1.08	1.31	1.17	1.14	1.15	1.09	1.19
$\varepsilon_{max}\,(\%)$	> 10	< 10	< 10	-	~ 10	~ 10	~ 10

Note that ε_{max} is the maximum absolute deviation of the seven fitting errors; these seven are the average absolute fitting deviations within the low and intermediate ranges of frequencies, ε_1 and ε_2, the differences in local rheological features $\Delta\omega_{1c}$, $\Delta G'_{1c}$, $\Delta G''_{1c}$, and $\Delta\omega_{mid}$, as well as in the error in predicted solution viscosity $\Delta\eta_0$. (See Fig. S4 for definitions of these fitting deviations/errors). By varying $\bar{Z}$ from its unconstrained best-fit value, the insensitivity percentage for $\bar{Z}$ is determined by the variation in $\bar{Z}$ for which ε_{max} first achieves 10%.

Table S2. The same as Table S1, except for the sensitivity of l_e at the imposed values listed in the top row; the corresponding fits are shown in Fig. S6b.

Parameters	50% l_e	75% l_e	90% l_e	Best-fit	115% l_e	130% l_e	160% l_e
$\bar{Z}$	3.00	2.88	2.85	2.83	2.83	2.75	2.62
$l_e\,(nm)$	213	302	362	403	463	524	645
$l_p\,(nm)$	70.5	39.8	33.2	30.1	25.5	21.2	15.0
ς	54	171	167	178	196	170	67
$G_N\,(Pa\cdot s)$	17.24	16.66	14.86	13.77	13.11	13.11	13.63
$\langle L\rangle\,(\mu m)$	0.64	0.87	1.03	1.14	1.31	1.44	1.69
$\varepsilon_{max}\,(\%)$	>> 10	> 10	~ 10	-	< 10	< 10	< 10

Table S3. The same as Table S1, except for the sensitivity of l_p at the given imposed values; the corresponding fits are shown in Fig. S6c.

Parameters	50% l_p	70% l_p	90% l_p	Best-fit	110% l_p	130% l_p
$\bar{Z}$	2.62	2.74	2.78	2.83	2.80	2.88
$l_e\,(nm)$	645	508	421	403	372	316
$l_p\,(nm)$	15	21.1	27.1	30.1	33.1	39.2
ς	67.3	102	120	178	142	140
$G_N\,(Pa\cdot s)$	13.63	13.94	14.43	13.77	14.23	15.59
$\langle L\rangle\,(\mu m)$	1.69	1.39	1.17	1.14	1.04	0.91
$\varepsilon_{max}\,(\%)$	< 10	< 10	< 10	-	~ 10	> 10

Table S4. The same as Table S1, except for sensitivity of ς at the given values; the corresponding fits are shown in Fig. S6d.

Parameters	ς/64	ς/16	ς/4	Best-fit	2ς	4ς	8ς
$\bar{Z}$	3.26	2.99	2.85	2.83	2.80	2.81	2.79
$l_e\,(nm)$	497	451	410	403	418	413	405
$l_p\,(nm)$	24.8	28.2	29.5	30.1	29.1	29.6	29.3
ς	2.5	10	40	178	320	640	1280
$G_N\,(Pa\cdot s)$	10.3	12.15	13.72	13.77	13.44	13.5	14.13
$\langle L\rangle\,(\mu m)$	1.62	1.35	1.17	1.14	1.17	1.16	1.13
$\varepsilon_{max}\,(\%)$	>> 10	> 10	< 10	-	< 10	< 10	< 10

Table S5. The same as Table S1, except for sensitivity of G_N at the given values; the corresponding fits are shown in Fig. S6e.

Parameters	75% G_N	85% G_N	95% G_N	Best-fit	105% G_N	110% G_N	120% G_N
$\bar{Z}$	2.80	2.87	2.83	2.83	2.81	2.82	2.82
$l_e\,(nm)$	162	171	155	178	137	173	203
$l_p\,(nm)$	539	449	441	403	391	383	333
ς	24.8	29.3	27.5	30.1	30.4	30.1	34.4
$G_N\,(Pa\cdot s)$	10.32	11.7	13.08	13.77	14.45	15.14	16.52

$\langle L \rangle$ (μm)	1.51	1.29	1.25	1.14	1.1	1.08	0.94
ε_{max} (%)	> 10	~ 10	< 10	-	< 10	~ 10	> 10

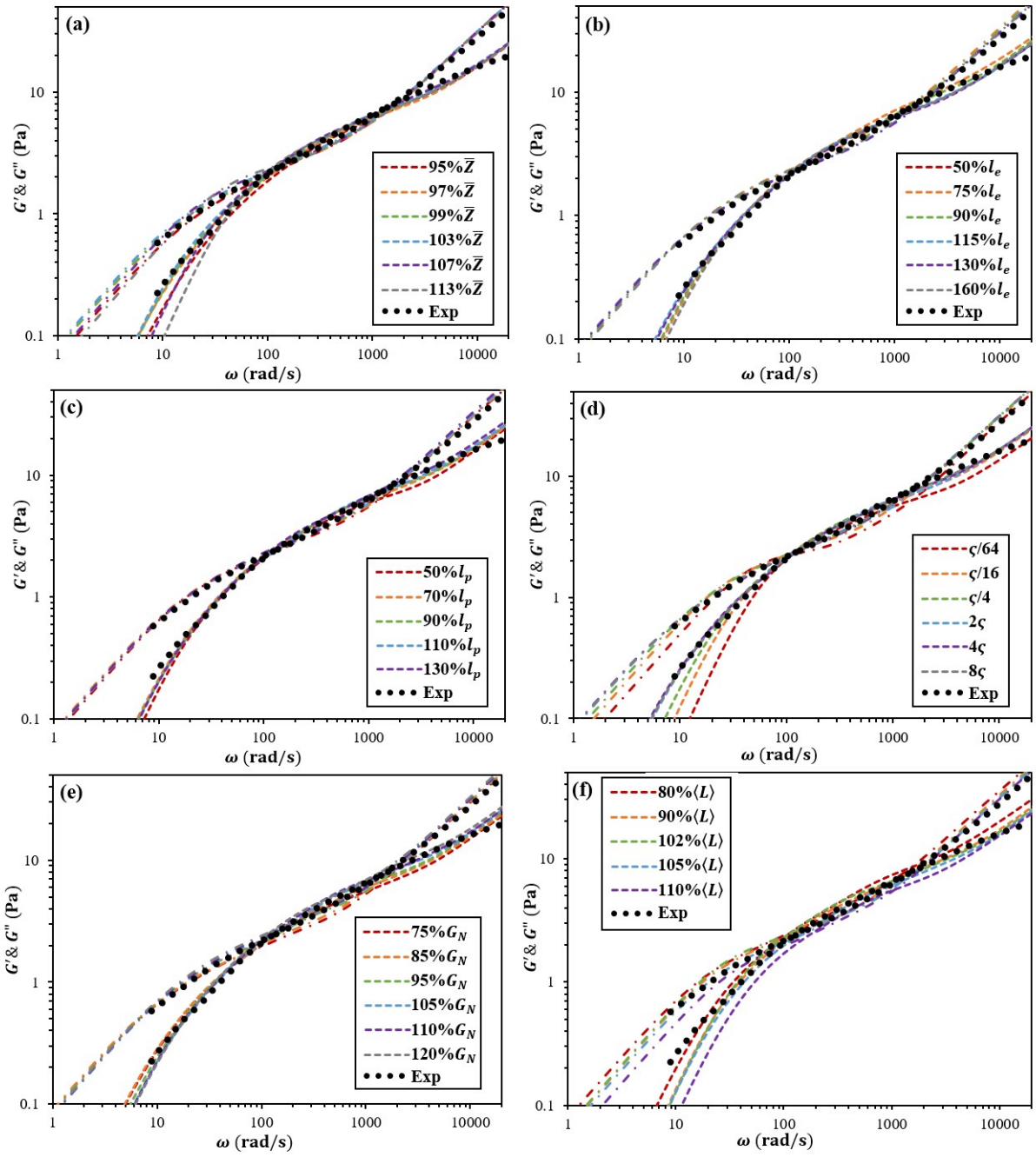

Figure S6. Fitting results showing sensitivity of best fits to imposed value of (a) $\bar{Z}$; (b) l_e; (c) l_p; (d) ς; (e) G_N; (f) $\langle L \rangle$ for partially entangled WLM solution with corresponding fitting parameters given in Table S1-6.

Table S6. The same as Table S1, except for sensitivity of $\langle L \rangle$ at the given values; the corresponding fits are shown in Fig. S6f.

Parameters	80% $\langle L \rangle$	90% $\langle L \rangle$	Best-fit	102% $\langle L \rangle$	105% $\langle L \rangle$	110% $\langle L \rangle$
$\bar{Z}$	2.87	3.07	2.83	3.11	2.80	2.56
$l_e\ (nm)$	318	336	403	373	429	488
$l_p\ (nm)$	45.2	41.3	30.1	34.5	29.6	27.9
ς	65.3	14.2	178	10.5	25.6	24.8
$G_N\ (Pa \cdot s)$	15.69	13.14	13.77	13.44	12.59	10.74
$\langle L \rangle\ (\mu m)$	0.912	1.03	1.14	1.16	1.20	1.25
$\varepsilon_{max}\ (\%)$	~ 10	< 10	-	< 10	~ 10	> 10

Table S7. Parameter values obtained by best fitting rheological data with fixed l_p= 32 nm, for sensitivity study of $\bar{Z}$ at the given values; the corresponding fits shown in Fig. S7a.

Parameters	95% $\bar{Z}$	97% $\bar{Z}$	99% $\bar{Z}$	Best-fit	101% $\bar{Z}$	103% $\bar{Z}$	107% $\bar{Z}$
$\bar{Z}$	2.67	2.73	2.79	2.83	2.83	2.90	3.02
$l_e\ (nm)$	409	400	391	403	399	379	377
ς	190	280	178	178	186	68.2	58.3
$G_N\ (Pa \cdot s)$	12.5	13	13.6	13.77	13.1	14.3	14.5
$\langle L \rangle\ (\mu m)$	1.09	1.09	1.09	1.14	1.13	1.1	1.14
$\varepsilon_{max}\ (\%)$	~ 10	< 10	< 10	-	< 10	~ 10	> 10

Table S8. The same as Table S7, except for sensitivity study of l_e at given values; the corresponding fits are shown in Fig. S7b.

Parameters	85% l_e	90% l_e	95% l_e	Best-fit	102% l_e	105% l_e	110% l_e

$\bar{Z}$	2.84	2.85	2.85	2.83	2.76	2.91	2.82
$l_e\,(nm)$	343	362	382	403	410	422	444
ς	311	210	149	178	100	162	112
$G_N\,(Pa\cdot s)$	17.2	15.5	14.1	13.77	14.13	11.8	10.8
$\langle L\rangle\,(\mu m)$	0.975	1.03	1.09	1.14	1.13	1.23	1.25
$\varepsilon_{max}\,(\%)$	> 10	> 10	~ 10	-	< 10	~ 10	> 10

Table S9. The same as Table S7, except for sensitivity study of ς at given values; the corresponding fits are shown in Fig. S7c.

Parameters	ς/64	ς/16	ς/4	Best-fit	2ς	4ς	8ς
$\bar{Z}$	3.27	3.03	2.88	2.83	2.77	2.81	2.84
$l_e\,(nm)$	455	419	389	403	379	384	395
ς	2.5	9	35	178	280	560	1120
$G_N\,(Pa\cdot s)$	10.33	11.95	13.65	13.77	14.32	14.01	13.29
$\langle L\rangle\,(\mu m)$	1.49	1.27	1.12	1.14	1.05	1.08	1.12
$\varepsilon_{max}\,(\%)$	>> 10	> 10	~ 10	-	< 10	< 10	< 10

Table S10. The same as Table S7, except for sensitivity study of G_N at given values; the corresponding fits are shown in Fig. S7d.

Parameters	85% G_N	90% G_N	95% G_N	Best-fit	105% G_N	110% G_N	115% G_N
$\bar{Z}$	2.88	2.87	2.86	2.83	2.81	2.81	2.76
$l_e\,(nm)$	424	411	399	403	377	367	359
ς	170	32.3	88.2	178	175	157	173
$G_N\,(Pa\cdot s)$	11.7	12.4	13.1	13.77	14.5	15.1	15.8
$\langle L\rangle\,(\mu m)$	1.22	1.18	1.14	1.14	1.06	1.03	0.991
$\varepsilon_{max}\,(\%)$	~ 10	< 10	< 10	-	~ 10	~ 10	> 10

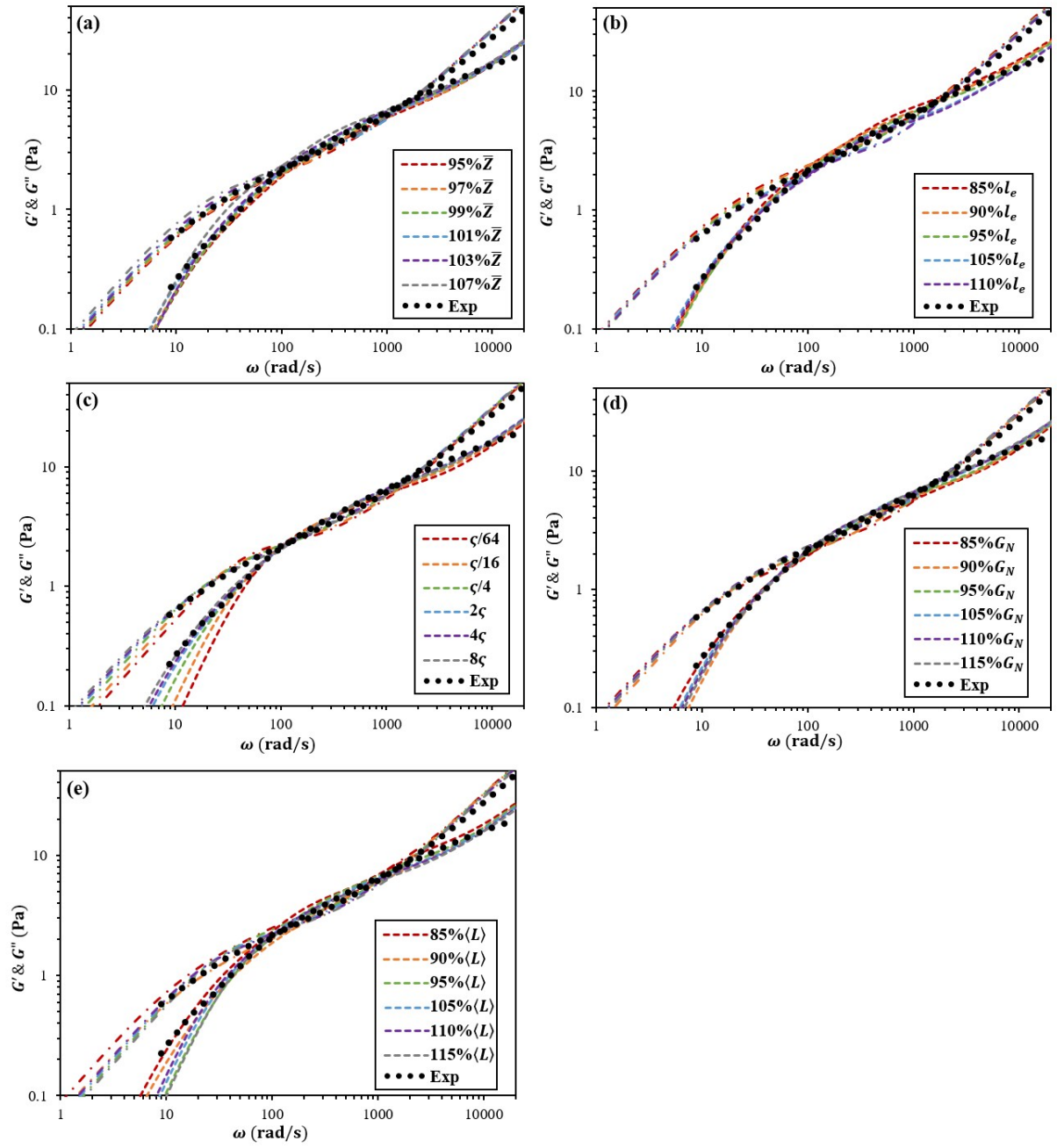

Figure S7. Fitting results showing sensitivity of best fits to imposed value of (a) $\bar{Z}$; (b) l_e; (c) ς; (d) G_N; (e) $\langle L \rangle$ for partially entangled WLM solution with corresponding fitting parameters given in Table S7-11.

Table S11. The same as Table S7, except for sensitivity study of $\langle L \rangle$ at given values; the corresponding fits are shown in Fig. S7e.

Parameters	85% $\langle L \rangle$	90% $\langle L \rangle$	95% $\langle L \rangle$	Best-fit	105% $\langle L \rangle$	110% $\langle L \rangle$	115% $\langle L \rangle$
$\bar{Z}$	2.85	2.62	2.87	2.83	2.98	3.01	3.05
$l_e\,(nm)$	339	389	376	403	400	415	430
ς	589	749	15.2	178	14.3	13.6	7.05
$G_N\,(Pa \cdot s)$	17.5	13.7	14.5	13.77	13	12.2	11.4
$\langle L \rangle\,(\mu m)$	0.965	1.02	1.08	1.14	1.19	1.25	1.31
$\varepsilon_{max}\,(\%)$	> 10	~ 10	~ 10	-	< 10	< 10	~ 10

Detailed Expressions for ς_{DC}. According to O'Shaughnessy and Yu,[63] after a breakage event (at $t = 0$) the recombination probability would approach unity at $t = \bar{\tau}_{rec}$, i.e., the average time for two newly created micelle ends to recombine is:

$$\int_0^{\bar{\tau}_{rec}} dt \cdot \frac{k_{rec} b^3}{x(t)^3} \approx \frac{\bar{\tau}_{rec} k_{rec} b^3}{x\left(\bar{\tau}_{rec}\right)^3} \cong 1 \qquad (S3)$$

Here k_{rec} is the recombination rate of two overlapping micelle ends of size b, and $x(t)$ is the root mean square displacement of a micelle end after time t. We can take $x(t) \sim t^{1/2}$ both for unentangled micelle rods due to translational diffusion and for entangled WLMs at late times due to center of mass diffusion when micelles can escape from their original tubes, while, following O'Shaughnessy and Yu, we obtain $x(t) \sim t^{1/4}$ for entangled WLMs as a result of reptation in the tube (which is itself a random walk in space) at early times. Since at equilibrium, the overall recombination rate should equal the breakage rate, therefore:

$$k_{rec} b^3 c_{end}^{\ 2} = c_{end} / \bar{\tau}_{br} \qquad (S4)$$

where $c_{end} \equiv 1/\langle h \rangle^3$ is the density of micelle ends, and

$$\langle h\rangle \equiv \sqrt[3]{\frac{\langle L\rangle \pi d^2}{(8\phi)}} \qquad (S5)$$

$\langle h\rangle$ is defined as the average distance between any two micelle ends. Given ϕ=1.51% and d=4 nm, for the two entangled WLM solutions considered in the main text, i.e., [Na+]=0.601 M (partially entangled with $\langle L\rangle$=1.14 μm, see Fig. 7b) and [Na+]=0.852 M (well entangled with $\langle L\rangle$=5.90 μm, see Fig. 7b), $\langle h\rangle$ equals 78 nm and 135 nm, respectively. For the two unentangled solutions (ϕ=0.20%), i.e., [Na+]=0.586 M ($\langle L\rangle$=488 nm, see Fig. 7b) and [Na+]=0.983 M ($\langle L\rangle$=3.10 μm, see Fig. 7b), $\langle h\rangle$ equals 115 nm and 214 nm, respectively. Since $\bar{\tau}_{rec}$ is related to $x(\bar{\tau}_{rec})$ through either reptation (for entangled solutions at early times), center of mass diffusion (for entangled solutions at late times), or translational diffusion (for unentangled solutions),

$$x(\bar{\tau}_{rec})^2 \sim \begin{cases} a\langle L_t\rangle \cdot (\bar{\tau}_{rec}/\bar{\tau}_{rep})^{0.5} & by\ reptation \quad (S6a) \\ \bar{\tau}_{rec} \cdot D_G & by\ center\ of\ mass\ diffusion \quad (S6b) \\ \bar{\tau}_{rec} \cdot D_t & by\ translational\ diffusion \quad (S6c) \end{cases}$$

With

$$D_c = \frac{k_B T \cdot ln(l_e^{3/5} l_p^{2/5}/d)}{2\pi\eta_s\langle L\rangle};\ D_G = \frac{D_c}{3\bar{Z}};\ D_t = \frac{k_B T \cdot ln(\langle L\rangle/d)}{2\pi\eta_s\langle L\rangle} \qquad (S7)$$

Here, D_c, D_G, and D_t are curvilinear, center of mass, and translational diffusivity (of a short cylindrical micelle), respectively, for a micelle with average length $\langle L\rangle$. η_s is the solvent viscosity. $\bar{\tau}_{rep}$ ($=\langle L_t\rangle^2/\pi^2 D_c$) is the reptation time, while $\langle L_t\rangle$ and a ($=\sqrt{2 l_e l_p}$) are the tube length and tube diameter, respectively.[32] Equations S6b and c are simple relationships for three dimensional diffusion. Equation S6a is for diffusion along the random-walk trajectory of the tube, which controls the micelle diffusion at times less than $\bar{\tau}_{rep}$. To obtain Eq. S6a, note that the curvilinear distance $x_c(\bar{\tau}_{rec})$ traveled by the micelle along the tube is related to the time for reaction by

$x_c(\bar{\tau}_{rec})^2 \sim D_c\tau_{rec}$, and that the distance traveled in real space $x(\bar{\tau}_{rec})$ is related to the curvilinear distance traveled (along the random walk with step size a) by $x(\bar{\tau}_{rec})^2 \sim a\, x_c(\bar{\tau}_{rec})$. From these equations and the formula for $\bar{\tau}_{rep}$ we get Eq. S6a.

With the diffusion distance of micelle ends set by $\langle h\rangle$, the diffusion time $\bar{\tau}_D$ can be determined by solving the following equations for either entangled or unentangled solutions:

$$\langle h\rangle^2 = \begin{cases} a\langle L_t\rangle \cdot (\bar{\tau}_D/\bar{\tau}_{rep})^{0.5} & for\ entangled\ solutions \\ \bar{\tau}_D \cdot D_t & for\ unentangled\ solutions \end{cases} \qquad (S8)$$

Note that once micelles are entangled, $\langle h\rangle \cong l_e < \langle L\rangle$; therefore within $\langle h\rangle$, the diffusion of micelle ends is dictated by reptation. With $a \cdot \langle L_t\rangle = \langle L\rangle \cdot 2l_p$, combining Eqs. S3~S8, it follows that:

$$\varsigma_{DC} \equiv \frac{\bar{\tau}_D}{\bar{\tau}_{rec}} = \begin{cases} \left(\dfrac{\bar{\tau}_D}{\bar{\tau}_{br}}\right)^4 & for\ entangled\ solutions\ at\ short\ times \\ \left(\dfrac{\bar{\tau}_{br}^{2/3}\bar{\tau}_{rep}^{1/2}}{\bar{\tau}_D^{1/6}\bar{\tau}_G}\right)^3 & for\ entangled\ solutions\ at\ long\ times \\ \left(\dfrac{\bar{\tau}_{br}}{\bar{\tau}_D}\right)^2 & for\ unentangled\ solutions\ at\ all\ times \end{cases} \qquad (S9)$$

where $\bar{\tau}_G$ ($\equiv 2l_p\langle L\rangle/D_G$) is the time for center of mass diffusion over the average end-to-end distance of a micelle of average length $\langle L\rangle$. Given T=298.2 K, η_s=1.2 mPa.s, and d=4 nm, for partially entangled WLM solutions at [Na+]=0.601 M: $\langle L\rangle$=1.14 μm, l_p=32 nm, (see Fig. 7) and $\langle h\rangle$=78 nm (from Eq. S8), we obtain $\bar{\tau}_{rep}$=12.5 ms, $\bar{\tau}_D$= 87.4 μs, and $\bar{\tau}_G$=0.373 s. By the same token, for well entangled WLM solutions at [Na+]=0.852 M: $\langle L\rangle$=5.90 μm, l_p=57 nm, (see Fig. 7) and $\langle h\rangle$=135 nm (from Eq. S8), $\bar{\tau}_{rep}$=3.18 s, $\bar{\tau}_D$= 2.34 ms, and $\bar{\tau}_G$=94.1 s.

From the breakage times in Fig. 6f and Eq. S9, for the partially entangled solution ($\bar{\tau}_{br}$=1.45 s), assuming that recombination reaction occurs at early times gives ς_{DC}=1.31×10^{-17}. Since $\varsigma_{DC} \equiv \bar{\tau}_D/\tau_{rec}$ and $\bar{\tau}_D$= 87.4 μs, this implies that $\bar{\tau}_{rec}$ is far too long to be self-consistent with the early-time assumption for recombination. Hence, we can safely take the late time formula for this solution. Doing so gives ς_{DC}= 6.06. This implies that the mean-field theory is marginal, or beginning to fail for this solution. If we use this value to compute the distance $x(\bar{\tau}_{rec})$ that the micelle ends diffuse before recombining, we get $x(\bar{\tau}_{rec})$=49.8 nm, which is of order the average separation distance between micelle ends at this concentration. Thus, a freshly created micelle end typically is able to find and fuse with its original partner micelle about as easily and some other micelle can do so. For the well-entangled solution ($\bar{\tau}_{br}$=0.82 s), however, ς_{DC}=6.63×10^{-11} at early times and 9.46×10^{-5} at late times. Thus, ς_{DC} for the well entangled solutions is found to be far less than unity no matter whether the early- or late-time diffusion is assumed, indicating that micelle breakage and re-formation are deeply within the MF limit. The tiny values of ς_{DC} at early times given above are too extreme because they are based on the $t^{1/4}$ scaling of diffusion distance with time, which is no longer valid at long times at which the micelles can escape from their tubes and can diffuse with a $t^{1/2}$ power. By time they do this, however, ς_{DC} increases to a much larger value at late time but still within the MF regime for the well-entangled solution, since the diffusion distance has become much greater than the average distance between micelle endcaps (i.e., $\langle h \rangle$~100 nm). It therefore becomes much more likely for different micelles to fuse with the fragments of a broken micelle than for the two pieces of a broken micelle to self-recombine. The relatively long time for two newly formed ends to recombine with each other is a consequence of the low probability of recombining during the very brief time intervals in which they are close enough to

fuse (of order ~5 nm separation). As time passes, and they fail to self-recombine, they diffuse farther and farther out of this small range, and the time required for them to find each other again, to have a new chance to fuse, becomes ever longer. Unless the concentration is dilute or the micelles are short, another micelle within this range will have already fused with the partner fragment well before self-recombination can occur. Thus, because the probability of recombining per encounter is rather low, the chance of self-recombination of the two fragments of a broken micelle is small.

Knowing $\bar{\tau}_{br} \sim 1/\langle L \rangle$ from thermodynamics of micelle aggregation[65] we can also calculate ς_{DC} for dilute solutions (ϕ=0.20% SLE1S+CAPB, T=298.2 K, η_s=1.2 mPa.s, and d=4 nm), whose length scales are estimated by SANS as shown in Fig. 7a and b. For example, at [Na+]=0.586 M: $\langle L \rangle$=488 nm (from Fig. 7) and $\langle h \rangle$=115 nm (from Eq. S8); at [Na+]=0.983 M: $\langle L \rangle$=3.10 μm (from Fig. 7) and $\langle h \rangle$=214 nm (from Eq. S8), we obtain $\bar{\tau}_D$= 2.46 ms and $\bar{\tau}_{br}$=3.39 s for [Na+]=0.589 M and $\bar{\tau}_D$= 39.14 ms and $\bar{\tau}_{br}$=1.56 s for [Na+]=0.983 M, respectively. (Note that the above values of $\bar{\tau}_{br}$ are determined by assuming a constant breakage rate for unit length of micelle at fixed ionic strength.) Thus, the obtained ς_{DC} (i.e., 1.38×10^6 at [Na+]=0.589 M and 1.59×10^3 at [Na+]=0.983 M, see Eq. S9) for the unentangled solutions are found to be far larger than unity, indicating that micelle fusion is diffusion controlled and self-recombination dictates the relaxation.

From Eqs. S7~S9, and $a \cdot \langle L_t \rangle = \langle L \rangle \cdot 2l_p$, Equation S9 can also be rewritten in a detailed form as:

$$\varsigma_{DC} \equiv \begin{cases} \left[\dfrac{d^{8/3}\langle L\rangle^{4/3}}{32\pi^{2/3}\phi^{4/3}\cdot l_e l_p D_c\cdot \bar{\tau}_{br}}\right]^4 & for\ entangled\ solutions\ at\ short\ times \\ \left[\dfrac{2^{1/3}\phi^{2/9}D_c^{2/3}\cdot \bar{\tau}_{br}^{2/3}}{3\pi^{8/9}d^{4/9}\cdot \bar{Z} l_e^{1/3} l_p^{1/3}\langle L\rangle^{2/9}}\right]^3 & for\ entangled\ solutions\ at\ long\ times \\ \left[\dfrac{4\phi^{2/3}D_t\cdot \bar{\tau}_{br}}{\pi^{2/3}d^{4/3}\langle L\rangle^{2/3}}\right]^2 & for\ unentangled\ solutions\ at\ all\ times \end{cases} \quad (S10)$$

Since $\bar{\tau}_{br} \equiv 1/(k_{br}\langle L\rangle)$ (k_{br} is the breakage rate per unit length of micelle), $D_c, D_t \sim 1/\langle L\rangle$, and assuming $l_e \sim \langle h\rangle \sim \sqrt[3]{\langle L\rangle/\phi}$ as well as $\langle L\rangle \sim \phi^{\nu}$, Eq. S10 can be simplified as:

$$\varsigma_{DC} \equiv \begin{cases} \left(\dfrac{\langle L\rangle^3}{\phi}\right)^4 \sim \phi^{4(3\nu-1)} & for\ entangled\ solutions\ at\ short\ times \\ \left(\dfrac{1}{\langle L\rangle^{4/3}}\right)^3 \sim \phi^{-4\nu} & for\ entangled\ solutions\ at\ long\ times \\ \left(\dfrac{\phi^{2/3}}{\langle L\rangle^{8/3}}\right)^2 \sim \phi^{\frac{4}{3}(1-4\nu)} & for\ unentangled\ solutions\ at\ all\ times \end{cases} \quad (S11)$$